

Distribution of Noise Sources For Noise Derived Green's Functions

Nicholas Harmon¹, Catherine Rychert², Peter Gerstoft³

¹National Oceanography Centre, University of Southampton, UK

²University of Bristol, Bristol, UK

³Scripps Institution of Oceanography, University of California, San Diego, USA

Abstract

We demonstrate that the distribution of seismic noise sources affects the accuracy of Green's function estimates, and therefore isotropic and anisotropic tomographic inversions for both velocity and attenuation. We compare three methods for estimating seismic noise source distributions, and quantify the potential error in azimuthal anisotropy and attenuation estimates due to inhomogeneous source distributions. The methods include: 1) beamformer output, 2) a least-squares inversion of year long stacked noise correlation functions (NCF) assuming both a 2-D plane wave source density model, and 3) a 3-D plane wave source density model.

We use vertical component data from the 190 stations of the Southern California Seismic Network and some USArray stations for 2008. The good agreement between the three models suggests the 2-D plane wave model, with the fewest number of unknown parameters, is generally sufficient to describe the noise density function for tomographic inversions. At higher frequencies, 3-D and beamforming models are required to resolve peaks in energy associated with body waves, and beamforming provides higher resolution.

We assess anisotropy and attenuation uncertainties for the noise source distribution in southern California by inverting isotropic lossless synthetic Fourier transformed NCF predictions based on modelled 2-D source distribution for these quantities. We find that the variation in phase velocity with azimuth from inhomogeneous source distribution yields up to 2% peak-to-peak anisotropy. For uncertainty in attenuation coefficients we predict values on the same order as the expected attenuation, making noise attenuation extraction challenging. To avoid biased results, we recommend that noise correlation studies reporting attenuation and anisotropy incorporate source density information.

Keywords: Surface Waves, Interferometry, Attenuation, Anisotropy

1 Introduction

Ambient noise surface wave tomography has improved the resolution of the crustal and upper mantle velocity structure (Sabra *et al.*, 2005, Shapiro *et al.*, 2005). However, discrepancies exist between isotropic phase velocity inversions of noise derived empirical Green's functions (EGF) and inversions of teleseismic data at the same periods. There is a bias in the EGF data in the average phase velocities, typically $< 1\%$, which after tomographic inversion of station-to-station phase into 2-D phase velocity maps leads to a bias in the phase velocities on the order of a few percent (Yang *et al.*, 2008, Yao *et al.*, 2006, Yao and Van Der Hilst, 2009). An inhomogeneous source distribution is a potential cause of this bias.

Although the effect of inhomogeneous source distributions on isotropic velocity estimates is likely within the error bars of these studies, it may have a more significant impact on higher-order

earth models, i.e., those reporting attenuation and anisotropy. For instance, a systematic variation in phase with azimuth due to an inhomogeneous source distribution could easily be mapped into estimates of azimuthal anisotropy. For attenuation studies, an inhomogeneous source distribution causes variations in the amplitude of the NCF, which must be accounted for to properly examine attenuation structure. In addition, modelling the variation in amplitude with distance of the NCF directly depends on the dimensionality of the distribution of sources (Aki and Richards, 2002), i.e. whether the expected amplitude falls off with station-to-station distance, s , as $1/s$ in the 3-D case, where the EGF recovered is a point source, or as $1/\sqrt{s}$ in the 2-D case where the far-field EGF recovered is a line source.

The first question to consider when solving for noise source distribution is dimensionality. In other words are sources confined to the surface of the earth (2-D) or distributed throughout its volume (3-D)? As shown by Harmon *et al.* (2008) and Ekstöm *et al.* (2009), the NCF is largely dominated by surface waves which is an azimuthally dependent, 2-D distribution of sources confined to the surface of the Earth. However, at some frequencies there may be noise sources that contribute to the EGF that travel across the seismic arrays at all incidence angles caused by scattering or body waves (Gerstoft *et al.*, 2008). The body waves are strongest in the upper part of the secondary microseism band. In other words, in the microseism band there may be a 3-D or azimuthal and incidence angle dependent distribution of sources.

In this paper we develop a method to estimate the distribution of noise sources, assuming either 2-D or 3-D source distribution, from the NCF and compare these methods to results from a noise source distribution obtained by beamforming on the NCF. The goal of estimating the noise source distribution is to then correct the phase velocity estimates from the NCF for the effects of an inhomogeneous source distribution and evaluate the uncertainty when sources are not taken into account. Using data from the Southern California Seismic Network and some of the USArray stations (which hereafter referred to as the extended SCSN) shown in Fig. 1, we examine the predicted effects on the amplitude and phase of the NCF for all three methods. With these observations we demonstrate to first order the distribution of noise sources at long periods is consistent with an azimuthally dependent 2-D distribution of noise, with the coherent sources travelling mostly as surface waves from the California coast. Using the best-fit model of the observed inhomogeneous noise field in the extended SCSN and the model's predicted synthetic NCF, we also evaluate the magnitude of the errors caused by the assumption of an isotropic noise field that could contribute to 1-D anisotropy and attenuation results.

2 Methods

We model the frequency domain NCF (FNCF) for both a 2-D and 3-D plane wave source density function using analytical expressions after Aki (1957) and Cox (1973). We use these expressions to set up the linear inverse problem, inverting the FNCF for the source density function. In addition, we detail a method for converting beamformer output to a 2-D amplitude density function. From these models we also derive expressions to predict the phase delay for a given inhomogeneous source distribution for any station-to-station path in an array. This phase delay can then be used to correct phase velocities used in tomographic inversions for source effects.

2.1 2-D source model

Following Cox (1973), the 2-D noise field frequency ω is described by a superposition of uncorrelated plane waves from all azimuths with a normalized amplitude density function, $A(\theta)$, of plane wave azimuth, θ .

The frequency domain correlation function (FNCF or R in eqs. 1-4) for two stations separated by distance s , station to station azimuth ζ , and phase velocity c can be obtained by integrating the phase delay of a plane wave between the stations over all azimuths weighted by the amplitude density function of $A(\theta)$:

$$R(\omega, s/c, \zeta) = \int_0^{2\pi} A(\theta) \exp\left(i\left(\frac{\omega s}{c}\right) \cos(\theta - \zeta)\right) d\theta \quad (1)$$

Expanding $A(\theta)$ in a Fourier series, the integral is recast as an infinite series (Cox, 1973):

$$\begin{aligned} R(\omega, s/c, \zeta) &= \sum_{m=0}^{\infty} i^m \varepsilon_m J_m\left(\frac{\omega s}{c}\right) [a_m(\omega) \cos(m\zeta) + b_m(\omega) \sin(m\zeta)] \\ &= a_0 J_0\left(\frac{\omega s}{c}\right) + 2 \sum_{m=1}^{\infty} i^m J_m\left(\frac{\omega s}{c}\right) [a_m(\omega) \cos(m\zeta) + b_m(\omega) \sin(m\zeta)] \end{aligned} \quad (2)$$

where ε is 1 when $m=0$, and 2 otherwise, and a_m and b_m are the Fourier coefficients of the amplitude density function. Note that for a uniform amplitude density, $R(\omega) \sim J_0(\omega s/c)$.

For a given noise field, described by its Fourier coefficients a_m and b_m , synthetic FNCFs can be computed for all station pairs in the array using Eq. (2). Conversely for observed FNCFs for all station pairs in an array, Eq. (2) can be used to linearly invert for the parameters a_m and b_m , using a truncated series of a small number of Fourier coefficients, see section 2.6.

2.2 3-D source model

For a 3-D distribution of plane waves the integral form of the FNCF is given by Eq. (43) in Cox (1973):

$$R(\omega, s/c, \xi, \gamma) = \int_0^\pi \int_0^{2\pi} A(\theta, \phi) \sin(\phi) \exp\left(i \frac{\omega s}{c} \sin(\phi) \sin(\gamma) \cos(\theta - \xi) + \cos(\phi) \cos(\gamma)\right) d\theta d\phi \quad (3)$$

where ϕ , is the incidence angle of the plane wave from the z axis in spherical coordinates, and γ is the station to station angle relative to the z axis. Similar to the 2-D case the FNCF is rewritten as a summation over the spherical harmonic expansion of $A(\theta, \phi)$ (Cox, 1973):

$$\begin{aligned} R(\omega, s/c, \xi, \gamma) &= \sum_{n=0}^{\infty} \sum_{m=0}^n i^n j_n \left(\frac{\omega s}{c}\right) P_n^m(\cos(\gamma)) [a_n^m \cos(m\xi) + b_n^m \sin(m\xi)] \\ &= a_0^0 j_0 \left(\frac{\omega s}{c}\right) + \sum_{n=1}^{\infty} \sum_{m=0}^n i^n j_n \left(\frac{\omega s}{c}\right) P_n^m(\cos(\gamma)) [a_n^m \cos(m\xi) + b_n^m \sin(m\xi)] \end{aligned} \quad (4)$$

Where γ is the station-to-station angle from the z axis in the spherical harmonic expansion, j_n is the spherical Bessel function, and P_n^m is the associated Legendre polynomial of order m, degree n, and a_n^m and b_n^m are the spherical harmonic coefficients of the amplitude density function $A(\theta, \phi)$. For uniform A, the integral of eq. 3 is proportional to the sinc function, $j_0(\omega s/c) = \sin(\omega s/c)/(\omega s/c)$. Again, the advantage of this parameterization is that it can be used to directly linearly invert the noise correlation function for the parameters a_n^m and b_n^m , with a truncated series of a small number of parameters, see section 2.6.

Assuming the stations lie on the surface of a flat Earth, therefore $\gamma=90^\circ$, eq. (4) is simplified:

$$R(\omega, s/c, \xi, \gamma) = a_0^0 j_0 \left(\frac{\omega s}{c}\right) + \sum_{n=1}^{\infty} \sum_{m=0}^n i^n j_n \left(\frac{\omega s}{c}\right) P_n^m(0) [a_n^m \cos(m\xi) + b_n^m \sin(m\xi)] \quad (4a)$$

where $m+n$ must be even. The assumed station geometry (stations lying in a plane) does not prevent us from detecting vertically incident plane waves, but the reduced resolution due to the station geometry and resulting truncation of the series means that only the longest wavelength features will be apparent.

This theory has two important ramifications: 1) These models predict that the amplitude decay for the 2-D model (J_0) in its asymptotic form ($\sqrt{(2c/\pi\omega s)} \cos(\omega s/c - \pi/4)$) is proportional to $1/\sqrt{s}$, while for the sinc function, the amplitude is proportional to $1/s$. 2) The proper way to extract the Green's function is based on the dimensionality i.e. in the 3-D case a time derivative of the NCF is needed or in the 2-D case a Hilbert transform with a $\pi/4$ correction is needed to estimate phase velocity for tomography. (Nakahara, 2006, Sanchez-Sesma and Campillo, 2006, Harmon *et al.*, 2007, 2008),

To apply these equations to real data we use the average phase velocity between each station-to-station pair (detailed in Sec. 2.4). We assume 1) The error in phase velocity is small 2) On average all station pairs have the same source distribution. 3) The source density function is

relatively smooth in azimuth 4) The FNCFs for different station pairs are recording data for approximately equivalent times. We assess these assumptions in subsequent sections.

2.3 Noise Correlation Function Calculation

We used the long period vertical records, sampled at 1 Hz from 190 stations of the SCSN array and some of the USArray stations in the Western US (Fig. 1) for Jan 1-Dec 31, 2008 (366 days). After removing the instrument response from the data, we bandpass filtered (0.02-0.30 Hz) and normalized the time series using the envelope. Using a 2^{18} point (one day) FFT the signals were whitened by Fourier coefficient normalization within the bandpass limits. For each frequency bin and for all station pairs, the NCF is computed and stacked for all possible days for all station pairs.

This processing makes the amplitude of the NCF comparable between station pairs because only the phase information is kept, i.e. the maximum amplitude at a given frequency is 1 for any one-day NCF. NCFs with the same number of days in the stack theoretically also have the same maximum amplitude, making comparison between NCFs straightforward. We present spectral data from NCF that have > 330 days stacked and have a station to station separation > 10 km. We normalized the real and imaginary components of the NCF spectra by the number of days in the stack. We use a cosine squared taper window on the NCF with a 20 s fall off each end of a 1600 s window centred on zero lag and Fourier transform the data.

Comparison of data between FNCF with different numbers of stacked days implicitly assumes that the variation of the noise source distribution between the FNCF with different numbers of stacked days was small. We assume that the $366-330=36$ days difference will contribute to the scatter in the data about the model, but will not be sufficient to obscure the overall picture. Further, 43% of the data have 366 days, and 70% have over 350 days. The difference between the noise fields for station pairs should average out because the days missing for many stations were scattered intermittently throughout the year. We repeated our experiments using only stations pairs with the maximum number of days (366) and found the model coefficients were within 95% confidence limits of the 330 days model estimate.

2.4 Phase Velocity Estimation

To estimate the average surface wave phase velocity (c in eqs. 1-4) for each station pair NCF we use the method of Harmon et al. (2008). In this method, with the observed NCF, the symmetric component of the time domain signal is calculated by summing the causal and acausal (time reversed) component of the NCF, which is equivalent to taking the Hilbert transform of the real component of the FNCF in the frequency domain. We can then determine the phase, θ , of the

symmetric component, which can then be used to calculate the phase velocity, $c = \omega / (\Theta + 2\pi n - \delta)$, where n is the number of spatial cycles, and δ is the phase shift due to the NCF source effects relative to a plane wave—typically assumed to be $-\pi/4$ for a homogeneous source distribution (Harmon *et al.*, 2008, Lin *et al.*, 2008, Yao *et al.*, 2006, Bensen *et al.*, 2007). The phase of each symmetric NCF was unwrapped and corrected for the phase for an isotropic 2-D noise field with a $\delta = -\pi/4$ phase shift. The cycle ambiguity was removed by matching the average phase velocity for the extended SCSN at 25 s from Yang *et al.* (2006). At the longest periods 25–40 s useable for our purposes, the average phase velocity from ambient noise is within $<1\%$ from the dispersion curve of Yang *et al.* (2006) derived from earthquakes using the two-plane wave approximation Rayleigh wave tomography method. Our phase velocities are used to project the data into distance/wavelength ($\omega s / (c2\pi)$) domain, assuming that our initial estimate is close to the effective velocity. By employing the station-to-station phase velocity we can account for the variations in wavelength caused by variations in velocity when solving for 2-D source distribution.

For the 3-D source model and the beamforming model the phase velocity for vertically incident waves will be different than the surface wave phase velocity. When inverting for 3-D source density functions, errors in the phase velocity due to higher body wave phase velocity will translate into mislocation in source density, i.e. there will be a trade off between incidence angle of a plane wave in the horizontal slowness term in eq. 3 ($\sin(\Phi)/c$). On the other hand, the beamforming method does not depend directly on the phase velocities determined here, but assumes a uniform phase velocity. This means that the beamforming method does take into account variations in earth structure, and may leak beamformer power into adjacent slowness and azimuths as different parts of the array become coherent near the true local slowness. The incidence angle ambiguity in both models could be resolved by assuming phase velocities appropriate for body waves.

2.5 Beamforming

Beamforming was performed using a 2^{12} sample fast Fourier transform of the >330 day stacked NCF similar to Gerstoft *et al.* (2007), without clipping of the signal. At each frequency, the Fourier transformed NCF forms a matrix $\mathbf{C}(\omega)$ containing the cross spectral density function of the array (FNCF) from the 190 stations used in the extended SCSN array. The plane wave response for the seismic array is given by $\mathbf{p}(\omega, c, \theta, \mathbf{r}) = \exp(i\omega(\mathbf{r}\mathbf{e})/c)$, where \mathbf{r} describes the coordinates of the array relative to the mean coordinates and \mathbf{e} contains the directional cosines of the plane wave. The beamformer output is given by: $b(\omega, c, \theta) = \mathbf{p}(\omega, c, \theta)^H \mathbf{C}(\omega) \mathbf{p}(\omega, c, \theta)$.

We searched for the maximum beamformer output, corresponding to the best-fitting plane wave, over slowness ($1/c$) from 0-0.40 s/km (2.5- ∞ km/s) and every 1° from 0-360 $^\circ$ azimuth. We note that similar results can be obtained for beamformer output by beamforming on shorter amplitude normalized time series and stacking the beamformer output.

2.6 Inverting FNCF for Source Density Functions

Assuming a 2-D source density function, eq. (2), we invert the real and imaginary components of all the normalized FNCF at a given frequency for the Fourier series expansion coefficients (a_m and b_m) which are assumed to be identical for all stations. We use the observed phase velocity and the station-to-station azimuth ζ and distance s to calculate the matrix of partial derivatives of R with respect to a_m and b_m , \mathbf{G} , as a function of $\omega s/c$ for each station pair. Thus \mathbf{G} will have dimension N_{pair} by $1+2K$, with N_{pair} being number of station pairs and K the model order. We use a least squares solution of the form:

$$\mathbf{M} = (\mathbf{G}^T \mathbf{G})^{-1} \mathbf{G}^T \mathbf{d} \quad (5)$$

where \mathbf{M} is the model vector of a_m and b_m , and \mathbf{d} is the complex-valued FNCF for all N_{pair} station pairs at a given frequency. We calculate the synthetic FNCF for the 2-D models after inverting for the best-fitting coefficients by calculating the best-fitting forward model using eq. (2) with the best estimates for average velocity between each station pair. Note that the derivatives of eq. (2) with respect to a_m and b_n form a well-conditioned inverse of $(\mathbf{G}^T \mathbf{G})$ and no regularization is required.

Similarly for the 3-D model, using eq. (4a), we take the derivatives of R with respect to a_n^m and b_n^m to form our matrix of partial derivatives. Again, no damping is required, because the partial derivatives of eq. (4) yield a well-conditioned inverse.

In order to transform the beamformer output to a source density function, the effects of the array geometry must be deconvolved from the beamformer output. The extended SCSN has a greater aperture in a roughly NW-SE direction, and will therefore have greater sensitivity and yield higher beamformer output in those directions. A simple way to address this problem is to recast beamforming in terms of a linear inverse problem in which the forward model is described either eqs. (1) or (3). Taking the simpler 2-D case and numerically approximating eq. (1) using the rectangle rule for numerical integration, \mathbf{G} becomes the matrix of partial derivatives of R with respect to $A(\theta_i)$, $\Delta\theta=1^\circ$, where subscripts i refers to the column, and j refers to the row of the matrix:

$$G_{ij}(s_j, \zeta_j, \omega, c, \theta_i) = \exp\left(i \frac{\omega s_j}{c} \cos(\theta_i - \zeta_j)\right) \Delta\theta \quad (6)$$

Thus \mathbf{G} will have dimension N_{pair} by 360.

In eq. (5), assuming \mathbf{d} is the complex valued vector of the NCF, the real component of $\mathbf{G}^T \mathbf{d}$ vector becomes related to the beamformer output at all azimuths at a given slowness ($1/c$) and frequency. The array response, or amplitude leakage across all azimuths for an input plane wave at a given θ_i is then given by the real component of $\mathbf{G}^T \mathbf{G}$. The deconvolution operator for the array response is given $(\mathbf{G}^T \mathbf{G})^{-1}$ and can be applied to the beamformer output at a given slowness.

In practice $\mathbf{G}^T \mathbf{G}$ is ill-conditioned and requires some regularization for stable inversion. We introduce a smoothing operator into our array response deconvolution operator $(\mathbf{G}^T \mathbf{G} + \mathbf{S})^{-1}$ where \mathbf{S} :

$$\mathbf{S} = \lambda \begin{bmatrix} 2 & -1 & 0 & 0 & 0 & \dots & -1 \\ -1 & 2 & -1 & 0 & 0 & \dots & 0 \\ 0 & -1 & 2 & -1 & 0 & \dots & 0 \\ \vdots & & & \ddots & & & \vdots \\ 0 & \dots & 0 & -1 & 2 & -1 & 0 \\ 0 & \dots & 0 & 0 & -1 & 2 & -1 \\ -1 & \dots & 0 & 0 & 0 & 2 & -1 \end{bmatrix} \quad (7)$$

We choose λ to be the largest eigenvalue of $\mathbf{G}^T \mathbf{G}$, which allows small oscillations in the $A(\theta)$ solution of the order $3\Delta\theta$ due to the structure of \mathbf{S} , for larger λ these oscillations are damped out. If the FNCF is inverted directly this approach has similarities to Yao and van der Hilst (2009). The deconvolution operator for the full beamformer output can be constructed for the 3-D model given in eq. (3) and could yield a more accurate estimate of the 3-D source density function if accurate body wave velocity information is included.

To examine surface wave source densities from the beamformer output we average over surface wave slownesses within ± 0.01 s/km from the slowness corresponding to the maximum beamformer output. We then apply the array response deconvolution operator to the average beamformer output to yield a 2-D estimate of the source density function.

2.7 Correcting Phase Velocity Estimates for Inhomogeneous Sources

Knowing the source density function, we can calculate the phase delay caused by inhomogeneous source distribution, and then correct the phase velocity estimate for each station-to-station path for this effect. Specifically, to determine the predicted phase shift, δ , relative to a plane wave caused by inhomogeneous source distribution we perform the same operations as we do on the observed data (see section 2.4). We first calculate of the symmetric component of the synthetic FNCF, by summing the Hilbert transform of the even terms (real terms) of eqs. (2) and (4) using the

fitted coefficients, a_m , and b_m , from the observed NCF. We then calculate the phase of the symmetric component and subtract the expected phase of a plane wave ($\omega s/c$).

Determining the phase shift of the symmetric component relative to a plane wave for the 2-D model is therefore given by summation over the even terms of m :

$$\delta(\omega, s/c, \xi) = \angle \left(\sum_{m=0}^{\infty} i^n \varepsilon_m \left(J_m \left(\frac{\omega s}{c} \right) + i Y_m \left(\frac{\omega s}{c} \right) \right) \left[a_m(\omega) \cos(m\xi) + b_m(\omega) \sin(m\xi) \right] \right) - \left(\frac{\omega s}{c} \right) \quad (8)$$

where δ is the predicted phase shift in radians and Y_m is the Bessel function of the second kind and \angle is the unwrapped angle of the symmetric component.

Similarly in 3-D summation over the even terms of n :

$$\delta(\omega, s/c, \xi) = \angle \left(\sum_{n=0}^{\infty} \sum_{m=0}^n i^n \left(j_n \left(\frac{\omega s}{c} \right) + i y_n \left(\frac{\omega s}{c} \right) \right) P_n^m(\cos(\gamma)) \left[a_n^m(\omega) \cos(m\xi) + b_n^m(\omega) \sin(m\xi) \right] \right) - \left(\frac{\omega s}{c} \right) \quad (9)$$

where y_n is the spherical Bessel function of the second kind. This phase difference is the required phase correction for the given source distribution.

In subsequent sections we present $\delta + \pi/4$, converted to cycles, which is the phase correction needed beyond the correction for an isotropic 2-D source distribution. We present the phase delay in this manner to highlight the azimuthal variation in phase delay, and this phase delay should have roughly 0 mean. This phase shift allows us to identify station-to-station azimuths and distances where the standard $-\pi/4$ do not apply. Assuming a homogeneous source distribution, a negative region might indicate where phase velocities is faster than the true velocity) and a positive regions where the phase velocity is slower than the true velocity. However, this does not remove the expected asymptotic behaviour in phase for large station-to-station distance of $-\pi/4$ and $-\pi/2$ corresponding to a uniform source distribution (i.e. Hilbert transforms of J_0 [for 2D] and j_0 [for 3D] which approach $-\pi/4$ and $-\pi/2$ relative to a plane wave respectively).

3 Investigation of Source Dimensionality (2-D vs. 3-D)

3.1 Zero Order Dimensionality Test: NCF as a Function of Station-to-Station Distance/Wavelength

We first examine whether the observed noise source distribution is 2-D (J_0 Bessel function) or 3-D (sinc). To accomplish this, we project the real component of the Fourier transformed NCF data into distance/wavelength (dimensionless wave number or number of spatial cycles of the wave) domain (Fig 2). This domain is preferable to station-to-station distance because it accounts for velocity variation (see section 2.4). We plot all station-to-station pairs in operation for over 330 days during 2008 and > 10 km apart, or 12485 data (grey dots in Fig. 2). As expected the data vary sinusoidally with respect to dimensionless wavenumber. Similar to Prieto et al. (2009), we average

the real component of the FNCF in distance/wavelength bins with a spacing of 0.1 and compare our data average to an amplitude normalized J_0 and sinc functions with respect to distance/wavelength, which are equivalent to the 0 order/degree coefficients in the modelling.

The phase and amplitude decay of the binned average of all data (black dashed in Fig. 2) with distance are best matched by J_0 (green line in Fig. 2) rather than a sinc function (red line in Fig. 2), at the longer periods with a correlation coefficient of .95 (.75 for a sinc) at 25 s, .94 (.76 for a sinc) at 28 s and .90 (.81 for a sinc) at 33 s period. Note that the correlation coefficient for J_0 and sinc function is 0.78 for the number of wavelengths used here. Our choice of phase velocity only impacts the phase of data, not the amplitude. Thus a different choice of phase velocity would affect the correlation coefficients (reducing the correlation with J_0), but the observed variation in amplitude is by inspection proportional to $1/\sqrt{s}$, consistent with the J_0 .

In the microseism band at 5 s (Fig. 2a) neither the J_0 nor the sinc function fit the data well, with correlation coefficients of 0.60 and 0.22, respectively. This is an indication that the source function is more complicated than either first order models would predict, and we will show later there is a strong body wave component in the beamformer output at 5 s period.

3.2 NCF as a function of Azimuth and Station-to-Station Distance/Wavelength

To investigate azimuthal variations in the FNCF data, we project and average the real and imaginary components of the NCF from all station pairs into 0.1 distance/wavelength and 1° azimuth bins (Fig. 3a,b). Here we consider a single period, 25 seconds, as an example case. This projection allows us to visualize the variation in amplitude with azimuth in the NCF caused by the noise source distribution. We observe a coherent pattern here, rather than random noise, suggesting that the entire array is seeing the same noise sources. To first order the data vary cyclically with increasing distance/wavelength for all azimuths for both the real and imaginary components as observed in Fig 2. There is a significant imaginary component to the data. In both the real and imaginary components, we observe a systematic variation in amplitude with azimuth, which corresponds to the scatter in the data shown in Fig. 2. The amplitudes of the real and imaginary components are larger in a roughly 290° azimuth, with the imaginary component showing asymmetry about the origin.

In Fig. 3c and as described in Sec. 2.7 we plot the azimuth and distance/wavelength binned and averaged phase shift, $\delta + \pi/4$, in cycles of the observed FNCF to highlight the azimuthal variation in phase shift caused by source heterogeneity at 25 s. There is azimuthal variation in the phase shift, with negative bands extending radially with an azimuth of 150° (-30°) and 22° (-158°), which are regions of faster than expected phase velocity. In-between there are regions of positive phase shift,

which correspond to slower phase velocity. There is some speckle in the phase shift likely caused by scattering and velocity variations across the region. Another feature in the phase data is at > 6 distance/wavelength the phase becomes strongly negative, particularly in the 90-180° quadrant which is due to a change in average velocity from the longer paths crossing to northern California.

Fig. 3 also shows a comparison of the predicted synthetic NCF and $\delta + \pi/4$ in cycles from the best-fitting 2-D (Fig. 3d,e,f), 3-D (Fig. 3g,h,i) and beamforming models (Fig. 3j,k,l); these will be described in Section 3.3.

3.3 Higher Order Source Models: Forward Models from Best-Fitting Source Distributions vs. Observations

We calculate the synthetic FNCF from our best-fitting amplitude density functions for the 2-D and 3-D source distribution models for an example period, 25 s (Fig 3d, e, g, h). In other words, we calculate the forward models shown in Figure 3 by using the best-fitting model coefficients a and b and $m = 8$ (2-D) and $n = 8$ (3-D) in equations 2 and 4 (see section 3.4, Fig. 4, and Tables 1 & 2 for description of the best-fitting amplitude densities). We assume a homogeneous isotropic phase velocity (3.65 km/s) across the region. For the beamforming model synthetic FNCF (Fig 3j, k), we numerically integrate eq. 1, using the best-fitting 2-D amplitude density function again assuming the same homogeneous isotropic phase velocity across the region. The predicted phase shifts of the 2-D and 3-D models (Fig. 3f, i) were calculated using eqs. 8 and 9 respectively, while the phase shift of the beamforming synthetics (Fig. 3l) was calculated from the phase of the Hilbert transform of the real component of the synthetic FNCF.

The synthetics derived from the three source distribution models match the observed FNCF well (Fig. 3). This is true for both the real and imaginary components, and particularly true from distance/wavelengths 0–3 where the amplitudes are highest. Specifically, all three models have a real component with higher amplitudes roughly in the E-W direction. The three models predict an imaginary component that has a similar magnitude but slightly less than the observed imaginary component, again with the highest amplitudes in a roughly E-W direction.

The phase shift of the 2-D and beamforming models matches the observed phase shift, but the 3-D model begins to shift in phase relative to the observations at wavenumbers > 3 . Comparison of the phase shift $\delta + \pi/4$, in cycles between the three models (Fig. 3f, 3i, 3l) and the observed data (Fig. 3c) shows that all three models pick up the reduced phase shift at $\sim -30^\circ$ and 22° azimuth. The magnitude of the negative phase is better represented in the 2-D model and the beamforming model. The 3-D model systematically under predicts the phase shift at distance/wavelength > 3 , approaching a $\delta + \pi/4$ of $-\pi/4$ (0.125 cycles) in fig 3i at large distance/wavelength, which when

combined the $-\pi/4$ phase shift accounted for in the figure is consistent with phase shift of the Hilbert transform of a sinc function ($-\pi/2$ or -0.25 cycles) relative to a plane wave.

The visual agreement of the pattern of the $\delta+\pi/4$ between the beamforming and 2-D models suggests a 2-D model is the most appropriate model at this period but there are significant differences in the predicted phase between the two models. Specifically, the beamforming model has a larger magnitude phase shift (-0.06 to 0.03 cycles relative to the expected 0.125 cycle shift required for a homogeneous distribution) at 22° and -30° azimuths relative than the 2-D model (-0.03 to 0.02 cycles relative to 0.125 cycles), and appears to match the observed phase better. If the 2-D model were calculated using $m>8$, the magnitude of the predicted phase shift increases slightly (± 0.01) but does not match the beamforming magnitude.

3.4 Predominantly 2-D (25 s Period) vs. 3-D (5 s period) Source Density Models

In this section we show the amplitude densities from the three source density modeling methods examined in this study for a 25 s period, which has a strong 2-D source distribution, and at 5 s which has a 3-D component to the data. We chose to show these two periods because they exemplify the two end member cases well and provide a means of examining the efficacy of our 3 modeling approaches under different conditions.

Fig. 4a shows the equivalent 2-D density functions for the three methods at 25 s and shows that the density functions are non-zero for all azimuths. At the longest wavelengths the three methods agree, requiring a large peak in the sources at 290° azimuth. As expected the 2-D and 3-D models produce nearly identical distributions. The beamforming amplitude density function, which has been allowed to go to the shortest wavelengths by our choice of smoothing, shows more structure, but is consistent with the other two models. For higher m , the 2-D model converges to the beamforming model. The beamformer output (Fig. 4c), shows much less structure than the 2-D models in the surface wave slowness region, highlighting the need to deconvolve the array response.

For 25 s period, the variance reduction between the three models is similar, with the models shown in Fig. 3 have maximum variance reductions of 67%. Fig. 4b shows the variance reduction the three models as a function of m for the 2-D model and n for the 3-D model relative to the beamforming model. The beamforming model fits the data better than the 0^{th} order/degree models but has 360 parameters (density every 1°), and maintains a better fit than the 3-D model until $n=8$. At $m=3$, the 2-D model explains the observations within 2% variance reduction beamforming model, so the models are nearly equivalent. At $m=n=6$ the 3-D model's variance reduction becomes equivalent to the 2-D model and increases slightly after that, however, the 3-D model requires 28

coefficients, relative to 13 coefficients needed to reach the same level of variance reduction for the 2-D model. We present the synthetics in Fig 3 d-1 with $m = n = 8$ for the 2-D and 3-D models because the variance reduction of all three models is the same for this number of coefficients.

The 2-D model and 3-D models are dominated by surface wave energy at 25 s period (Tables 1, 2 and Fig. 4c, 4d). The power of the coefficients for 25 s period for the 2-D model show that the $m=0,1$ terms are the largest. To account for the several orders of magnitude increase in the value of $P_n^m(0)$ at high order and degree and to show the relative importance of the power of the coefficients to each other, we present the 3-D coefficients multiplied by $P_n^m(0)$. For the 3-D model, the $n=0$ coefficient is significant but the same order of magnitude as some of the higher order harmonics ($n=2,m=0$ and $n=4,m=0$), suggesting the NCF is not produced by a 3-D noise source density.

The 3-D model is shown in Fig. 4d, and for comparison we show the normalized beamformer output in Fig. 4c. The 3-D source density function plot (Fig. 4d) is dominated by the high amplitude densities at horizontal to nearly horizontal angles (90°), and near zero amplitude densities in the vertical directions. The 3-D density function is symmetric in the upper and lower hemispheres, so we show only the lower hemisphere. The beamformer output (Fig. 4c) shows a similar pattern, with high beamformer output at slownesses corresponding to surface wave phase velocities. It is interesting to note, that the increase in beamformer output at $0.1 - 0.2$ s/km slowness, associated with body waves also appears to be present in the 3-D source density model.

At 5 s, where the strongest signal is from body waves arriving at high incidence angles, neither the 2-D nor the 3-D models adequately describe the data. In this period range the primary feature in the beamformer output are the peaks at slownesses < 0.1 s/km (Fig. 5 b). In the 3-D model (Fig. 5c), these peaks are broadened due to the truncation of the series at relatively low harmonics. There is some surface wave energy visible in the beamformer output, and Fig. 5a shows the equivalent 2-D source density function for the three models. The 2-D model and 3-D model accurately measure the surface wave energy, and are in general agreement with each other and the small peak observed in the beamformer 2-D model (Fig. 5a). In this period range the 2-D and 3-D models yield maximum variance reductions of 15% and 17% respectively. The influence of body waves causes the 2-D and 3-D models to break down, and therefore eq. (3) or a more realistic body wave velocity model must be used to invert for the 3-D source density function.

4 Discussion

4.1 Source Density Recovery

At longer periods (> 7 s), all three models recover noise source density functions that are dominated by surface waves. This is consistent with previous studies that have shown that the sources in

ambient noise are surface waves generated by ocean wave derived sources (Rhie and Romanowicz, 2006, Stehly et al., 2006, Tanimoto, 2007, Webb, 2008, Yang and Ritzwoller, 2008). Both the 3-D model and beamformer output show little energy coming from body waves (Fig 4c, d), so for ambient noise studies, a 2-D model is sufficient for characterizing the noise field in this period range.

At short periods, there does appear to be a significant body wave signal. As shown at 5 s in Fig 5, neither the 2-D nor 3-D models can cope with the body wave signals effectively due to the truncation of the finite series and incorrect velocity model in the 3-D case, and the violation of the 2-D assumption for the 2-D model. For detection of vertically incident noise sources, the beamforming method provides the highest resolution of the three methods tested. However, to recover accurate amplitude density information, an assumption about the velocity structure must be made to convert from slowness to incidence angle.

4.2 Predicted Phase Shifts

At long periods, the 2-D, 3-D and beamforming methods predict similar surface wave source density functions, with similar fits to the data, but the 3-D model does not match the observed phase shift well. The 3-D model has a significant sinc function component and it matches observed amplitudes well, but there is a substantial phase shift between the 2-D and 3-D models for > 3 distance/wavelength or cycles (Fig. 3f, 3i). This phase shift is not observed in the data (Fig. 3c), which has an average of ~ 0.125 cycles for wavenumbers < 4 . The apparent error in the phase shift of the 3-D model, likely reflects errors introduced by truncation of the series for the 3-D model and the loss of the odd harmonics due to the station geometry. This suggests that the 2-D models and beamforming models are better for characterizing the source density function and predicting phase shifts at longer periods.

The azimuthal pattern between the 2-D and beamforming models predicted phase shift is similar but there is a difference in the magnitude. Some of the differences in the magnitude of the predicted phase shift between the 2-D and beamforming models (Fig. 4a) may be due to earth structure and scattering. The 2-D model accounts for Earth structure somewhat by taking the average phase velocity between station pairs, but as discussed by Tsai (2009) and Yao and Van Der Hilst (2009), Earth structure outside the station-to-station path may also introduce small phase delays. There may be some error in the 2-D model estimate of the required phase shift presented, and may require an iterative approach with complete regional velocity tomography similar to Yao and Van Der Hilst (2009) to readjust the phase velocity at each iteration. On the other hand, the beamforming model assumes an average velocity across the array. Although averaging over

slowness in the beamformer output should help to reduce the effects of heterogeneity somewhat. The small (<1%) difference in variance reduction between the 2-D model and the beamforming model suggests the long wavelength source density function may be sufficient for characterizing the phase shifts in the data due to source effects. We prefer the 2-D model for long periods because it requires the least number of parameters, and has a more accurate velocity model, which gives the most conservative estimate for δ .

4.3 Effects of Inhomogeneous Source Density on Isotropic and Anisotropic Phase Velocity

The source density function from all three methods is inhomogeneous and produces an azimuthal trend in the phase shift of the symmetric FNCF. This will map into an azimuthal trend in phase velocity at a given distance/wavelength if the phase is only corrected for an isotropic source density function. For a mostly 2-D source distribution, the phase shift and phase velocity for symmetric component of the NCF has sinusoidal 2θ and 4θ azimuthal dependence from eq. 8. This is the same expected variation for azimuthal anisotropy if we assume Rayleigh wave azimuthal anisotropy of the form $c_0 + c_1\cos(2\theta-\psi_1) + c_2\cos(4\theta-\psi_2)$ after Smith and Dahlen (1973) where c_0 is the isotropic phase velocity, c_1 and c_2 are the anisotropic contributions to the phase velocity and ψ_1 and ψ_2 are the fast azimuth directions. Therefore, source inhomogeneity could be mapped into estimates of azimuthal anisotropy.

We illustrate the potential effects of inhomogeneous source on phase velocity estimates by mapping the synthetic phase shift, $\delta + \pi/4$, in figure 3f to phase velocity. We then solve for c_0 , c_1 and ψ_1 at a given distance/wavelength in the Smith and Dahlen (1973) model, ignoring the 4θ terms. We plot our results in Fig. 6 a, b, c for 1, 3, and 4 distance/wavelength, respectively. The phase is calculated using the symmetric component, so the phase velocity curves repeat every 180° of azimuth because they have an inherent 2θ , 4θ , 6θ and 8θ variation due to the even terms in eq. (8).

For a 1-D isotropic phase velocity study which solves only for c_0 , the azimuthal variation in phase shift observed in Fig. 3f at 25 s period would be averaged resulting in an isotropic mean phase velocity that is 0.1 to 0.9% higher than the true phase velocity (3.65 km/s) going from 4 to 1 cycles or distance/wavelength. The increased velocity results from an average phase shift of -0.128 cycles at 1-4 distance/wavelength, which is a direct result of both the asymptotic behavior of the phase of J_0 at low distance/wavelength and the inhomogeneous source density. In this case, the noise derived average phase velocity is faster than the assumed phase velocity, suggesting that in practice the $\pi/4$ correction in most cases slightly under corrects the phase. However, depending on

the station-to-station distance and azimuth distribution, this correction could also over predict the average phase and produce a slower than average isotropic phase velocity estimate.

If the observed range of phase difference in Fig. 3f for 25 s period is mapped into azimuthal variation of phase velocity, the -0.02 to 0.01 cycles phase difference from the isotropically distributed noise translates to a peak-to-peak variation of phase velocity of 2% down to 0% from 1-4 distance/wavelength or cycles. Most of the data at 25 s period lie within 1-4 distance/wavelength. In particular, at 3 distance/wavelength we find peak-to-peak anisotropy of 1%. This percentage is of the same order of the strength of anisotropy 4% observed in the region from SKS splitting (Liu *et al.*, 1995) and peak to peak anisotropy from surface waves of 1-2% (Yang and Forsyth, 2006). In this particular example, the variation has a strong 2θ periodicity (note the large coefficient in Table 1 at $m=2$), which could lead to a spurious apparent azimuthal anisotropy. Therefore, in this synthetic example, to minimize error in azimuthal anisotropy estimates without explicitly accounting for source effects, only station-to-station pairs whose distances are greater than 4x the wavelength should be used, which is in keeping with current practices. However, it is also possible that the Earth's anisotropic structure will map into source heterogeneity and full anisotropic velocity tomography may be needed in conjunction with source solutions to fully solve this problem as discussed by Yao and Van Der Hilst (2009).

4.4 Effect of Inhomogeneous Source Density on 1-D Attenuation Estimates

The amplitude of seismic signals depends on the distance from the source (geometric spreading), the source, scattering and focusing effects caused by velocity heterogeneity and intrinsic attenuation of the Earth. In order to extract information about the Earth's intrinsic attenuation from ambient noise studies, the effects of velocity heterogeneity, geometric spreading, and source should be accounted for. The 2-D model presented here provides a means of addressing the source and geometric spreading effects. Here we will illustrate the potential uncertainty in attenuation measurements caused by assuming an isotropic noise source distribution using synthetic, attenuation free data generated by inhomogeneous source distributions modeled from our southern California data.

The azimuthal variation of amplitude poses a problem for attenuation studies because uneven sampling across azimuths could lead to a biased 1D estimate of amplitude versus distance. Specifically, as we show for 25 s period in Fig. 3a, the station geometry used in this study preferentially samples NW trends, which is also roughly parallel to where the strongest gradients in the real component of the FNCF with azimuth occur. If estimates of 1-D attenuation were made using station pairs in a narrow azimuth range some of the source effects would be mitigated;

however, this would severely limit the number of observations. On the other hand, forming a 1-D attenuation estimate by sampling the real component of the FNCF over a broader range of azimuths across the azimuthal gradient in the FNCF would cause a 1-D variation with distance in amplitude not due to simple geometric spreading. Therefore, modeling this variation assuming a homogenous source distribution and assuming the zero order 2-D model with $1/\sqrt{s}$ geometric spreading, could lead to spurious estimates of intrinsic attenuation.

To estimate and illustrate the possible error due to sampling bias of the azimuthal variation and the assumption of an isotropic source density, we use the real component of the synthetic FNCF from our best-fit 2-D model at 7.5, 15, 20 and 25 s period, where $m=8$ and c is the empirically determined phase velocity from sec. 2.4 for each station-to-station pair. Again, the synthetic data are attenuation free. We estimate the attenuation coefficient, α , using a modified model of FNCF attenuation of Prieto *et al.* (2009) of the form:

$$R(\omega s/c) = A * (J_0(\omega s/c)) * \exp(-\alpha s) \quad (10)$$

where A is amplitude. We solve for A and α using a grid search fitting the synthetic data. We present the best-fitting α as our best estimate of the potential uncertainty with 95% confidence regions shown in Fig. 7.

From azimuthal variation and an assumed isotropic source density we estimate the total range of best-fitting α to be $0.2-1.1 \times 10^{-3} \text{ km}^{-1}$. At 20 s period $\alpha = 0.3 \times 10^{-3} \text{ km}^{-1}$ and at 15 s period $\alpha = 1.1 \times 10^{-3} \text{ km}^{-1}$, which are significant from zero. At 25 s period $\alpha = 0.2 \times 10^{-3} \text{ km}^{-1}$, and at 7.5 s, which has a nearly time invariant coastal noise source from the microseism, $\alpha = 0.5 \times 10^{-3} \text{ km}^{-1}$, although these are not significant from zero. However, we note that these values are the same order of magnitude as observed in Prieto *et al.*, (2009) ($0.27 - 6.4 \times 10^{-3} \text{ km}^{-1}$ from 25-5 s period); the larger values correspond to shorter periods.

These results indicate that the zero order 2-D model may be insufficient for describing the source effects in ambient noise studies, and that higher order models may be required to get accurate attenuation information. In addition, the effects of scattering and focusing may also play an important role especially at short periods, which are sensitive to shallow structure where strong velocity gradients may exist.

5 Conclusions

We investigated the effects of noise source distribution on 1-D isotropic and anisotropic phase velocity estimates and attenuation estimates. We determined the dimensionality and heterogeneity of noise source distributions in southern California by inverting the FNCF for 2-D and 3-D source

density functions using a 2-D plane wave model, a 3-D plane wave model, and beamforming. We find evidence for both 2-D and 3-D source distributions at different period ranges. At long periods (> 7 s) the noise field is effectively 2-D, therefore we prefer the 2-D plane wave model because it has the fewest number of parameters out of the three methods tested. At short periods (< 7 s) the noise field has a body wave component, which can only be resolved by the 3-D and beamforming models. However, the beamforming model has higher resolution and is our preferred method in this period range. For all periods the source density is not isotropic, indicating that estimates of phase velocity from the NCF will have a bias due to source effects and the amplitude of the FNCF will have an azimuthal dependence. We provide a means of quantifying the phase correction necessary for station-to-station noise cross correlation functions to recover accurate phase velocity estimates for accurate tomographic inversions. From synthetic NCF we quantify the potential biases in estimates of anisotropy and attenuation that arise from assuming an isotropic noise source density for NCF derived from an inhomogeneous density. Specifically, we estimate the bias in the isotropic phase velocity in southern California will be about 0.0-0.9% faster at 25 s, while the noise source distribution southern California can produce an azimuthal anisotropy up to 2%. Similarly, azimuthal changes in amplitude could be mapped into artificial attenuation yielding attenuation coefficients up to $1.1 \times 10^{-3} \text{ km}^{-1}$ at 15 s period. These error estimates illustrate the potential dangers of not accounting for inhomogeneous noise sources in ambient noise studies, and therefore we recommend that source density analysis be performed to mitigate and correct these biases.

6 References

- Aki, K., 1957. Space and time spectra of stationary and stochastic waves, with special reference to microtremors, *Bull. Earthq. Res. Inst.*, 35, 415-457.
- Aki, K. & Richards, P.G., 2002. *Quantitative Seismology*, 2 edn, Vol. 1, pp. 700, University Science Books, Sausalito, California.
- Bensen, G.D., Ritzwoller, M.H., Barmin, M.P., Levshin, A.L., Lin, F., Moschetti, M.P., Shapiro, N.M. & Yang, Y., 2007. Processing seismic ambient noise data to obtain reliable broadband surface wave dispersion measurements, *Geophys. J. Int.*, 169, doi: 10.1111/j.1365-1246X.2007.03374.x.
- Cox, H., 1973. Spatial correlation in arbitrary noise fields with application to ambient sea noise, *J. Acoust. Soc. Am.*, 54, 1289-1301.
- Ekström, G., Abers, G.A. & Webb, S.C., 2009. Determination of surface-wave phase velocities across USArray from noise and Aki's spectral formulation, *Geophysical Research Letters*, 36, L18301, doi:18310.11029/12009GL039131.
- Gerstoft, P., Shearer, P., Harmon, N. & Zhang, J., 2008. Global P,PP, and PKP wave microseisms observed from distant storms, *Geophys. Res. Lett.*, 35, L23306, doi:23310.21029/22008GL036111.
- Gerstoft, P. & Tanimoto, T., 2007. A year of microseisms in southern California, *Geophys. Res. Lett.*, 34, L20304, doi:20310.21029/22007GL031091.

- Harmon, N., Forsyth, D. & Webb, S., 2007. Using Ambient Seismic Noise to Determine Short-Period Phase Velocities and Shallow Shear Velocities in Young Oceanic Lithosphere *Bull. Seis. Soc. Am.*, 97, 2024-2039.
- Harmon, N., Gerstoft, P., Rychert, C.A., Abers, G.A., Salas de la Cruz, M. & Fischer, K.M., 2008. Phase velocities from seismic noise using beamforming and cross correlation in Costa Rica and Nicaragua, *Geophysical Research Letters*, 35, doi:10.1029/2008GL03587.
- Lin, F., Moschetti, M.P. & Ritzwoller, M.H., 2008. Surface wave tomography of the western United States from ambient seismic noise: Rayleigh and Love wave phase velocity maps, *Geophys. J. Int.*, doi:10.1111/j.1365-1246X.2008.03720.x.
- Liu, H., Davis, P.M. & Gao, S., 1995. SKS splitting beneath southern California, *Geophys. Res. Lett.*, 22, 767-770.
- Nakahara, H., 2006. Theoretical background of retrieving Green's function by cross-correlation: one-dimensional case, *Geophysical Journal International*, 165, 719-728.
- Prieto, G.A., Lawrence, J.F. & Beroza, G.C., 2009. Anelastic Earth structure from the coherency of the ambient seismic field, *J. Geophys. Res.*, 114, doi:10.1029/2008JB0006067.
- Rhie, J. & Romanowicz, B., 2006. A study of the relation between ocean storms and the earth's hum, *Geochem. Geophys. Geosyst.*, 7, doi:10.1029/2006GC001274.
- Sabra, K.G., Gerstoft, P., Roux, P., Kuperman, W.A. & Fehler, M.C., 2005. Surface wave tomography from microseisms in Southern California, *Geophys. Res. Lett.*, 32, doi:10.1029/2005GL023155.
- Sanchez-Sesma, F.J. & Campillo, M., 2006. Retrieval of the green's function from cross correlation: The canonical elastic problem, *Bull. Seis. Soc. Am.*, 96, 1182-1191.
- Shapiro, N.M., Campillo, M., Stehly, L. & Ritzwoller, M.H., 2005. High-resolution surface-wave tomography from ambient seismic noise, *Science*, 307, 1615-1618.
- Smith, M.L. & Dahlen, F.A., 1973. Azimuthal Dependence of Love and Rayleigh-Wave Propagation in a Slightly Anisotropic Medium, *J Geophys Res*, 78, 3321-3333.
- Stehly, L., Campillo, M. & Shapiro, N.M., 2006. A study of seismic noise from its long range correlation properties, *J. Geophys. Res.*, 111, B10206,doi:10.1029/12005JB004237.
- Tanimoto, T., 2007. Excitation of microseisms, *Geophys. Res. Lett.*, 34, L05308, doi:05310.01029/02006GL029046.
- Tsai, V.C., 2009. On establishing the accuracy of noise tomography travel-time measurements in a realistic medium, *Geophysical Journal International*, 178, 1555-1564.
- Webb, S.C., 2008. The Earth's Hum: the excitation of Earth normal modes by ocean waves, *Geophys. J. Int.*, 174, 542-566.
- Yang, Y. & Forsyth, D.W., 2006. Rayleigh wave phase velocities, small-scale convection, and azimuthal anisotropy beneath southern California, *J. Geophys. Res.*, 111, B07306, doi:07310.01029/02005JB004180.
- Yang, Y. & Ritzwoller, M.H., 2008. The characteristics of ambient seismic noise as a source for surface wave tomography *Geochem., Geophys., Geosys.*, 9, Q02008, doi:02010.01029/02007GC001814.
- Yang, Y., Ritzwoller, M.H., Lin, F.C., Moschetti, M.P. & Shapiro, N.M., 2008. The structure of the crust and uppermost mantle beneath the western US revealed by ambient noise and earthquake tomography, *J. Geophys. Res.*, 113, B12310, doi:12310.11029/12008JB005833.
- Yao, H. & Van Der Hilst, R., 2009. Analysis of Ambient Noise Energy Distribution and Phase Velocity Bias in Ambient Noise Tomography, with Application to SE Tibet, *Geophys. J. Int.*, 179, doi:10.1111/j.1365-1246X.2009.04329.x.
- Yao, H., Van der Hilst, R.D. & De Hoop, M.V., 2006. Surface-wave array tomography in SE Tibet from ambient seismic noise and two-station analysis: I - Phase velocity maps, *Geophys. J. Int.*, 166, p.732-744,doi: 710.1111/j.1365-1246X.2006.03028.x.

Table 1. 2-D Noise Model Power at 25 s Period

m	
0	0.113
1	0.034
2	0.020
3	0.011
4	0.006
5	0.003
6	0.0043
7	0.011
8	0.002

Table 2. Model Power 3-D at 25 s Period Normalized by $P_n^m(0)$

m\n	0	1	2	3	4	5	6	7	8
0	0.121	-	-	-	-	-	-	-	-
1	-	-0.102	-	-	-	-	-	-	-
2	0.115	-	0.076	-	-	-	-	-	-
3	-	0.068	-	-0.044	-	-	-	-	-
4	0.120	-	0.042	-	0.029	-	-	-	-
5	-	-0.065	-	0.025	-	-0.016	-	-	-
6	-0.081	-	0.042	-	-0.012	-	0.030	-	-
7	-	0.040	-	-0.007	-	0.006	-	-0.061	-
8	0.048	-	-0.013	-	0.019	-	-0.008	-	0.004

Figures

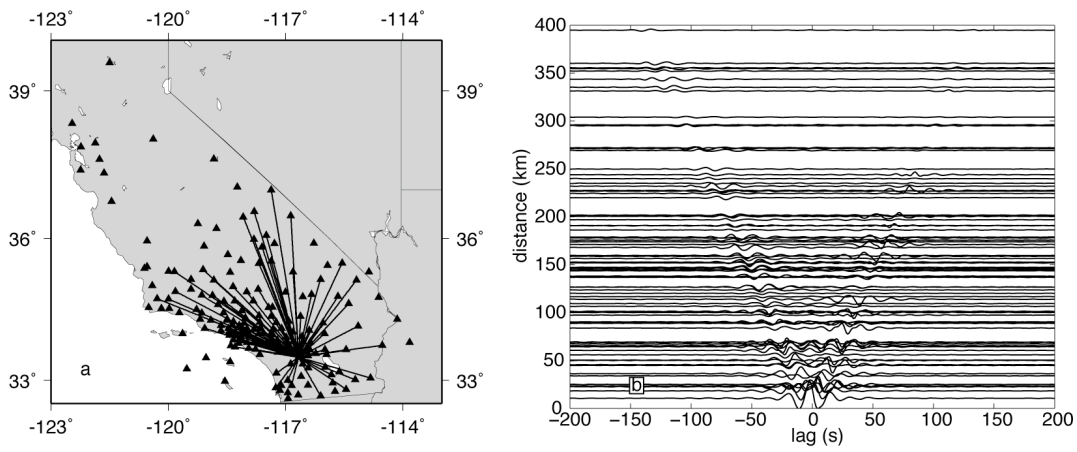


Figure 1. (a) Map of station locations (triangles) and station-to-station paths (solid) for sample record sections (b) plotted as a function of distance and lag. The sample record sections are bandpass filtered between 10-33 s.

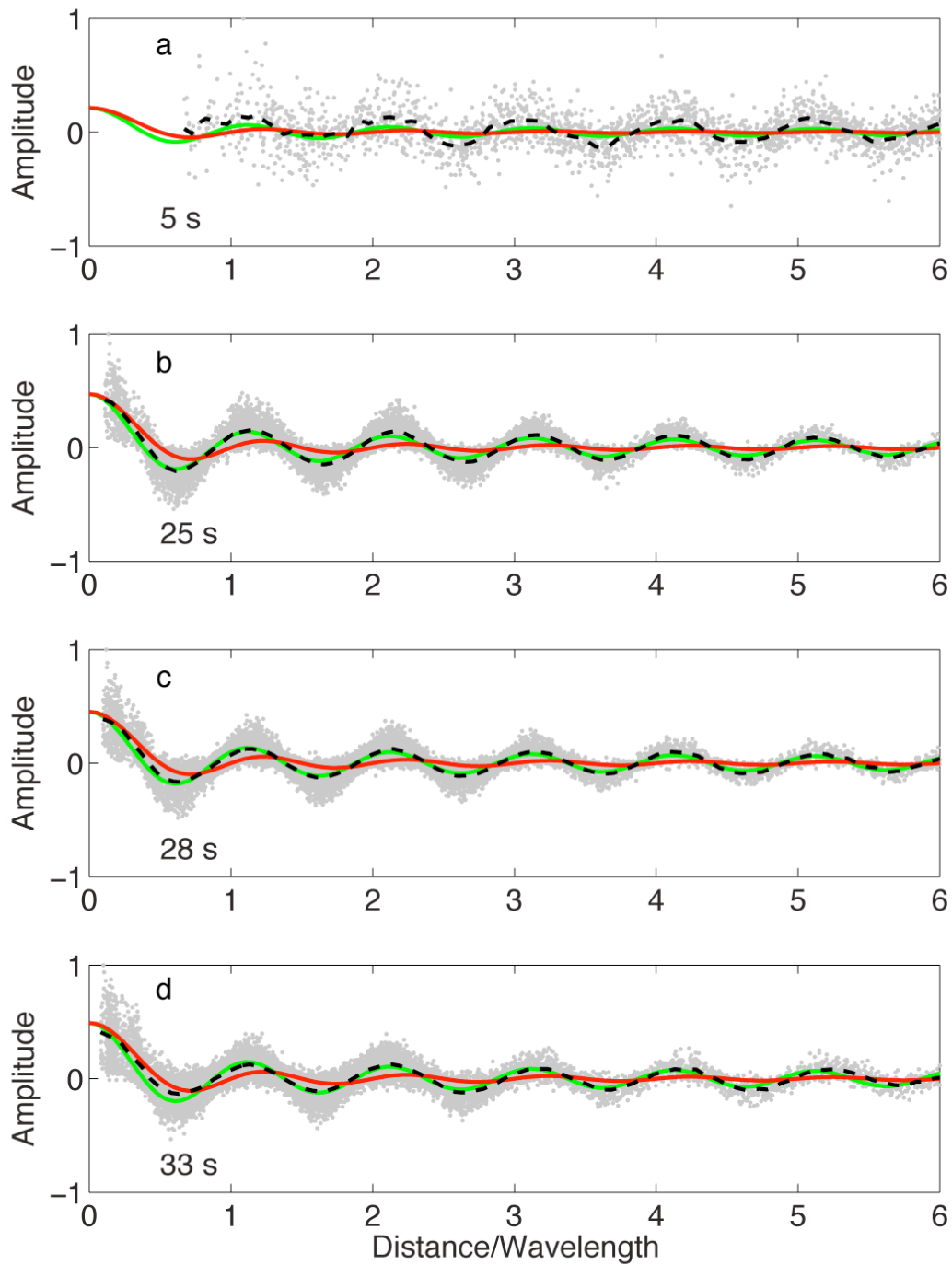


Figure 2. Real component of the Fourier transformed NCF (grey dots, normalized so the largest value is 1) as a function of dimensionless wavenumber (distance/wavelength) for 5 (a), 25 (b), 28 (c) and 33 (d) s period. The binned average of the data (black dashed line), $J_0(\omega s/c)$ (green) and sinc function (red) is also shown for each period.

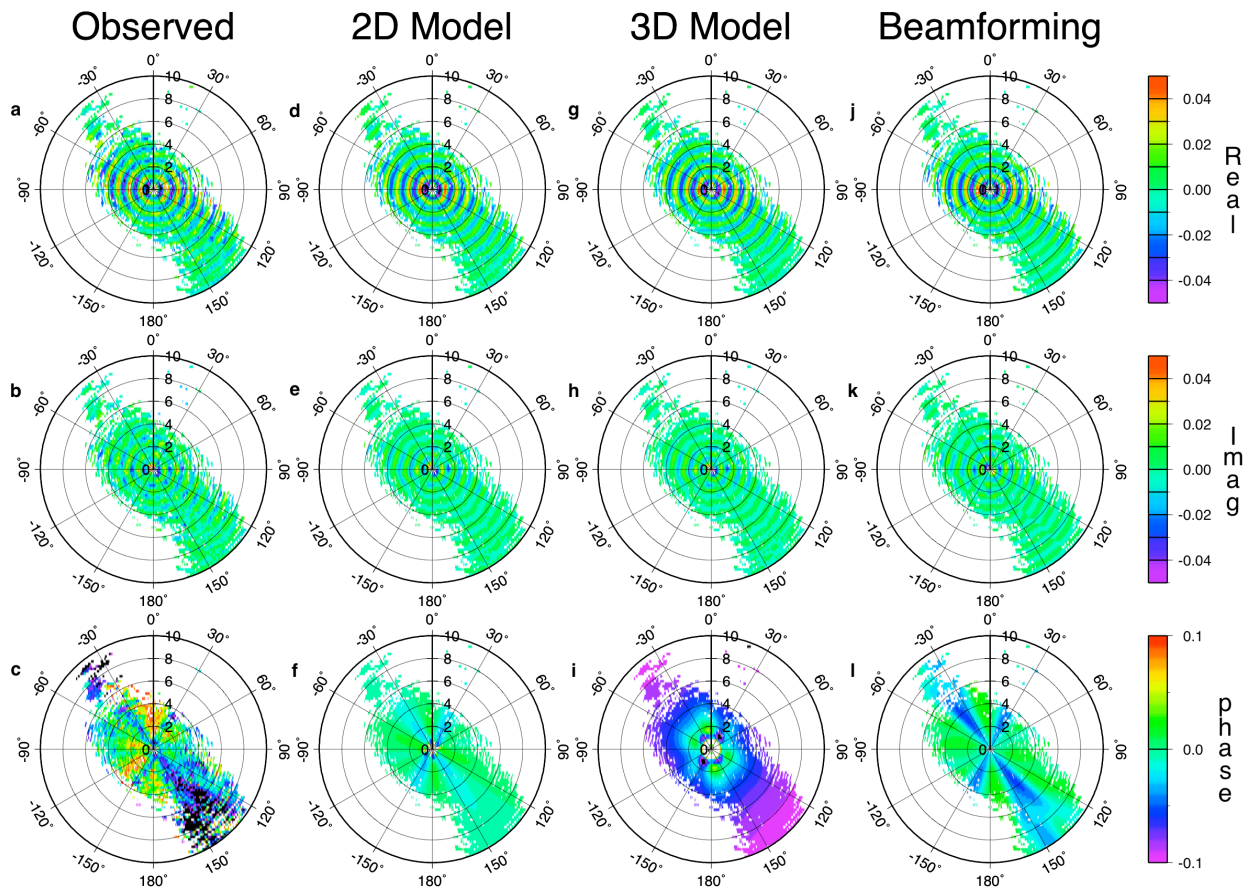


Figure 3. FNCF real (top row), imaginary (middle row) components and phase shift ($\delta+\pi/4$) in cycles (bottom row) of the observed (column 1 a,b,c), 2-D model (column 2 d,e,f), 3-D model (column 3 g,h,i) and beamforming (column 4 j,k,l) at a period of 25 s. The radial axis is distance/wavelength and azimuth is the angular axis.

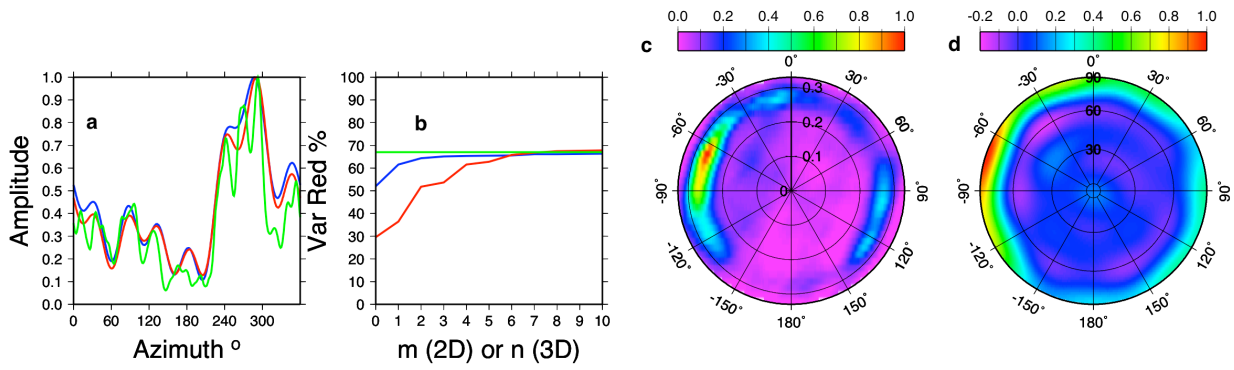


Figure 4. Comparison of the three methods at 25 s period. (a) 2-D (blue), 3-D (red) and beamforming (green) equivalent 2-D Source density functions, normalized to 1. (b) Variance reduction of the data (R^2) for the 2-D (blue), 3-D (red) and beamforming (green) source density functions. (c) Beamforming azimuth vs slowness and (d) 3-D model density function azimuth vs incidence angle.

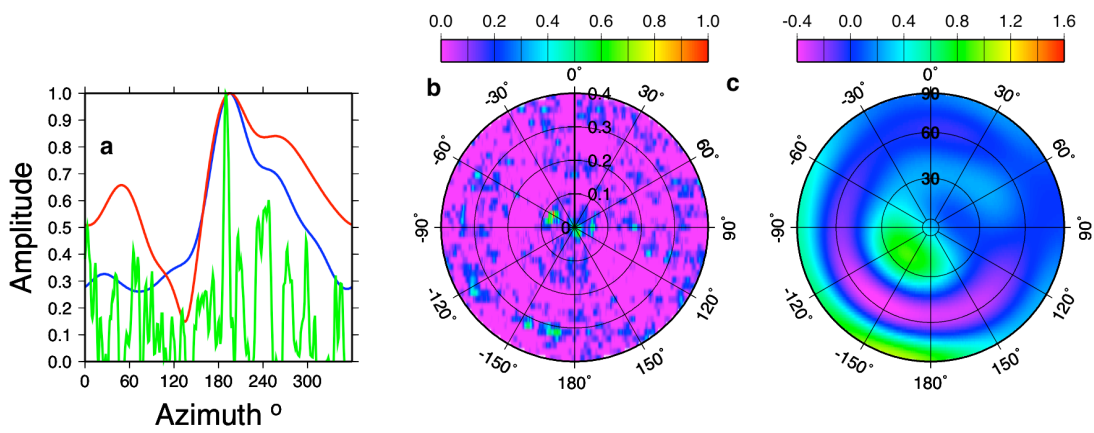


Figure 5. Comparison of the three methods at 5 s period. (a) 2-D (blue), 3-D (red) and beamformer (green) equivalent 2-D models. (b) beamforming azimuth vs slowness and (c) 3-D model density function azimuth vs incidence angle.

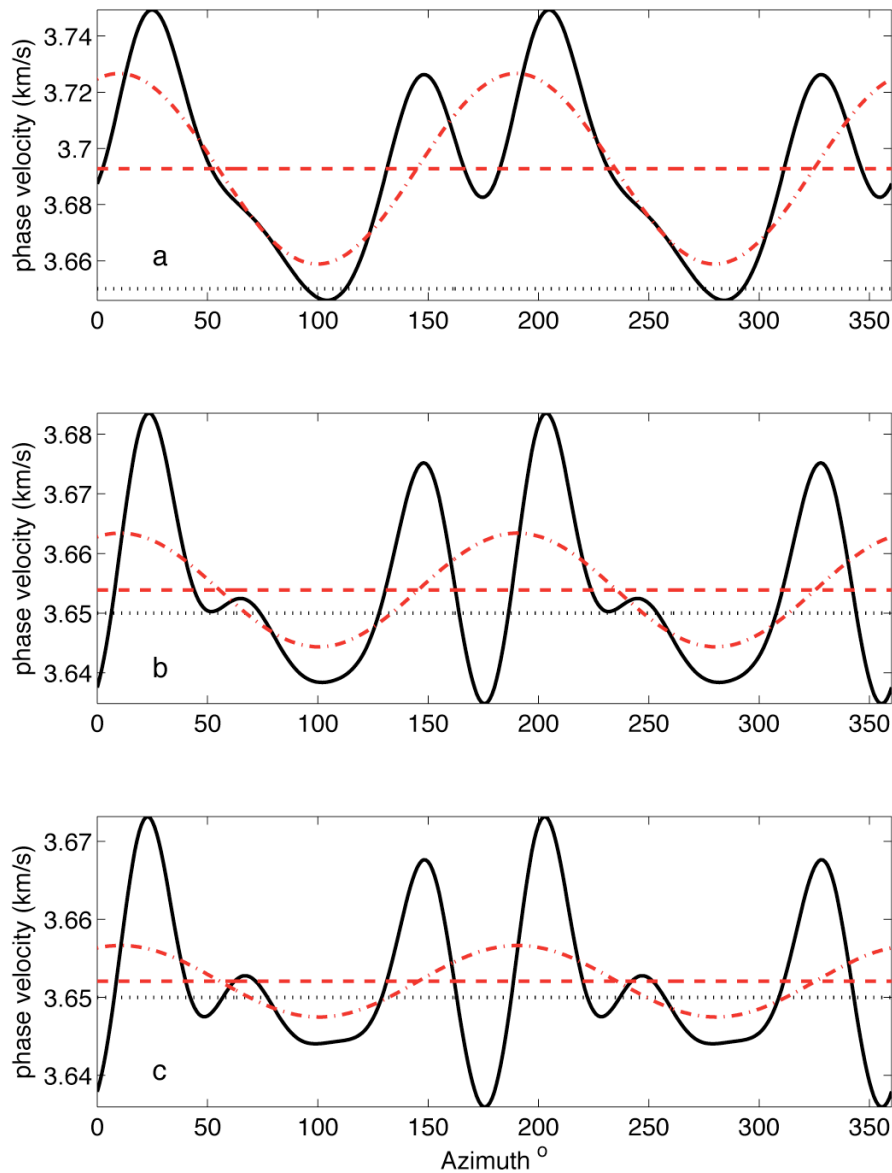


Figure 6. Synthetic FNCF phase shift at 25 s period (Fig 3f) mapped into apparent phase velocity (black line) due to inhomogeneous source at (a) 1, (b) 3 and (c) 4 distance/wavelength. The true phase velocity used for the calculation of the synthetics is shown as the dotted grid line at 3.65 km/s. Dashed red grid line shows the isotropic velocity (c_0) predicted from the phase velocity at those regions and the dashed-dotted red line shows the best-fitting 2θ anisotropy model ($c_0 + c_1 \cos(2\theta - \psi_1)$).

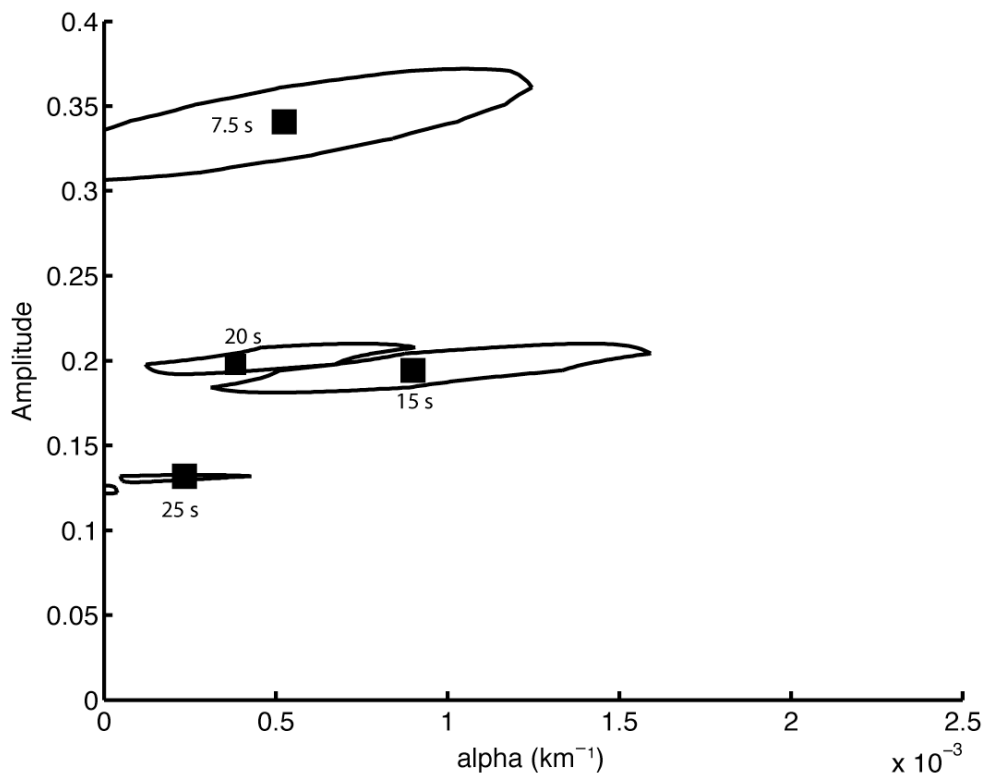


Figure 7. Grid search results for 1-D synthetic FNCF attenuation. Black squares indicate best-fitting α and A for period shown in label. Black line around squares indicate 95% confidence regions.